
Surface Reinforcement and Mechanical Behavior of Aluminum-Alloy Mechanical Arms for Logistics Robots

Calvin Whitmore

University of Texas at San Antonio, San Antonio, USA

cw2823@utsa.edu

Abstract: To enhance the hardness and tensile performance of aluminum-alloy mechanical arms used in logistics robots, WC-Ni composite powder was employed to fabricate coatings via single-track laser cladding, and tensile specimens were prepared using multi-track cladding. The experimental results indicate that as the laser power increases, the cladding layer height first increases and then decreases, while the molten pool depth continuously increases and the cladding width gradually expands. Meanwhile, the dilution rate initially decreases and subsequently increases. When the laser power reaches 1.0 kW, the single-track cladding layer exhibits the lowest dilution rate and achieves the most favorable metallurgical bonding with the substrate, indicating optimal coating-substrate compatibility. Phase composition analysis reveals that new phases, including W_2C , NiAl, Ni_3Al , M_7C_3 , and $M_{2-3}C_6$, are formed within the cladding layer. In terms of microstructural morphology, the top region of the cladding layer is dominated by fine cellular crystals; the middle region is enriched with a large number of WC particles as well as M_7C_3 / $M_{2-3}C_6$ carbides; and the bonding zone mainly consists of dendritic structures with pronounced directional characteristics. Mechanical property evaluation shows that the maximum microhardness of the single-track cladding layer reaches 960.6 HV, with hardness first increasing and then decreasing as the laser power rises. Regarding tensile performance, the coated specimens exhibit a tensile strength of 313 MPa and an elongation of 1.3%. Compared with the substrate material, the tensile strength is increased by 21.8%, while the elongation is reduced by 27.8%. In addition, multi-track laser cladding effectively improves the tensile fracture morphology and mitigates brittle fracture features at the coating-substrate interface, contributing to enhanced overall mechanical compatibility.

Keywords: laser cladding; robotic mechanical arm; microstructure; hardness; tensile properties

1. Introduction

At present, surface modification technologies include ultrasonic spraying [1], gas thermal spraying [2], sputtering [3], and laser cladding [4]. However, coatings produced by gas thermal spraying often suffer from poor wear resistance and limited controllability, while sputtered and ultrasonically sprayed coatings mainly rely on mechanical bonding with the substrate, resulting in low strength. Laser cladding overcomes these limitations. Emerging in the 1970s with the development of laser equipment, it has become a new type of surface modification technology [5-7]. Its principle is to melt alloy powders of high hardness, high strength, and strong corrosion and wear resistance using high-energy laser beams to rapidly form metallurgically bonded coatings with the substrate, thereby improving hardness, oxidation resistance, corrosion resistance, wear resistance, and overall mechanical performance [8-11].

Laser cladding features a narrow heat-affected zone, low dilution rate, high processing automation, and rapid cooling, which promotes refined microstructures and strong metallurgical bonding between the coating and the substrate. Cheng et al. investigated the influence of NiCr/TiAl coatings on the cladding of Ti600 titanium alloy and found that the grains in the coating were significantly refined, forming dendritic, cellular, and block-shaped microstructures. The maximum HV hardness reached 832, and the wear rate was lower than that of the substrate, substantially improving the alloy's wear resistance [12].

Common cladding powders include iron-base, nickel-base, and cobalt-base alloys. Ceramic-reinforced powders exhibit even higher strength, hardness, and wear and corrosion resistance, especially at elevated temperatures. Consequently, many researchers have added ceramic particles to alloy powders to further enhance coating hardness and strength [13-14]. Deng and colleagues applied Al₂O₃/NiCrAl composite coatings to ZL205A aluminum alloys and found that the prepared coatings exhibited uniform surfaces, stable thickness, and refined microstructures. The addition of Al₂O₃ ceramic particles significantly improved hardness and wear resistance while reducing coating loss [15]. Cheng et al. prepared CoMo/N/WC coatings on W18Cr4V tool steel and observed a metallurgical bond between the coating and the substrate, along with a continuous gradient microhardness distribution. Compared with the substrate, the coating demonstrated a notable hardness increase [16].

Ni60 alloy powder is a widely used nickel-base alloy powder characterized by high hardness, strength, wear resistance, and corrosion resistance. The B and Si elements in Ni60 powder promote deoxidation during cladding. In this study, aluminum alloy AISI10Mn is selected as the substrate for logistics robot mechanical arms, and WC-Ni60 composite coatings are applied. The analysis includes coating morphology, dilution rate, and hardness, as well as the mechanical properties of multi-track cladding tensile specimens. The results aim to provide a strengthening method for improving the performance of aluminum-alloy components in logistics robot mechanical arms.

2. Experiment

2.1 Preparation of Materials and Cladding Layers

The substrate material used in the experiment is AlSi10Mg aluminum alloy (its chemical composition is shown in Table 1). The dimensions of the single-track cladding specimens are 50 mm × 50 mm × 15 mm, and the multi-track cladding specimens have dimensions of $\phi 20$ mm × 100 mm. Prior to cladding, the substrate surface is polished with sandpaper to remove oxides, followed by ultrasonic cleaning in anhydrous ethanol to remove oil and impurities. The specimens are then preheated to 250 °C.

The cladding powder used in the experiment is WC-Ni60 powder, with particle sizes ranging from 45 to 10 μ m. The WC content is 20%, and the Ni60 powder composition is shown in Table 2. Before cladding, the powder mixture is placed in a vacuum drying oven for drying treatment, and afterward mixed with spherical hardening agent at a mass ratio of 8:1. A planetary ball mill is used for 5 hours with a rotational speed of 50 r/min. Stearic acid is used as a stabilizer to prevent agglomeration during ball milling.

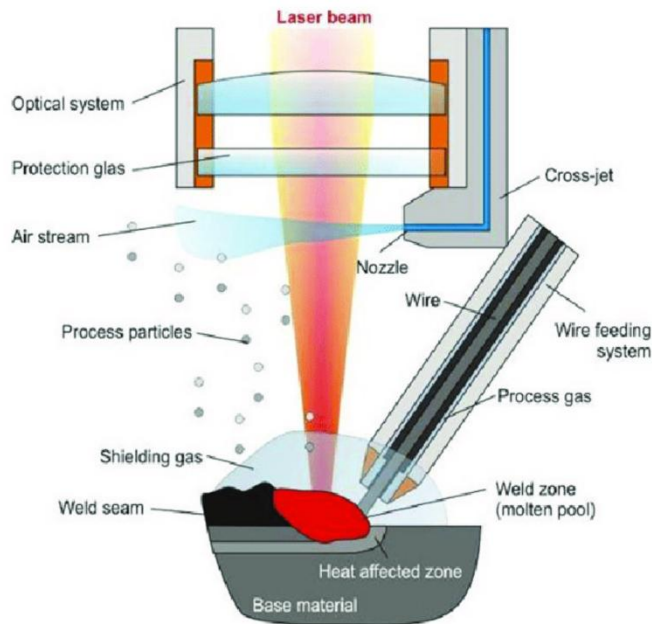
The experiment employs a YAG semiconductor fiber-laser processing system using a synchronous powder-feeding process. The laser cladding parameters are shown in Table 1. The laser powers used are 0.6, 0.8, 1.0, and 1.2 kW. The laser spot diameter is 3 mm, the powder-feeding rate is 15 g/min, and the scanning speed is 200 mm/min. High-purity argon is used as the shielding gas, with a gas flow rate of 25 L/min. During single-track cladding, the substrate must be placed on the side without laser heating to avoid laser reflection damage to nearby equipment. For multi-track cladding, the overlapping ratio is set to 50% with a rotational speed of 50 r/min.

Table 1: Chemical composition of AlSi10Mg alloy

Element	Al	Si	Mg	Fe	Cu	Mn	Zn
Mass fraction/%	Balance	10.5	0.26	0.64	0.15	0.28	0.14

Table 2: Chemical composition of Ni60 powder

Element	Ni	Cr	B	Si	Fe	C
Mass fraction/%	Balance	16.23	3.21	3.65	4.67	0.74

**Figure 1.** Schematic diagram of laser cladding

2.2 Characterization and Performance Testing

After natural cooling, the cladding specimens were cut using a DK7735 wire-cutting machine, ultrasonically cleaned with anhydrous ethanol, and mounted using an XQ-1 embedding machine. The mounted samples were ground with sandpapers of 74 μm and 23 μm grit sizes, followed by fine polishing with 13 μm , 6.5 μm , and 0.65 μm abrasive papers. Final polishing was performed using a polishing cloth. The samples were then etched using a mixed solution of HCl, HF, and HNO₃ at a volume ratio of 3:2:5, followed by ultrasonic cleaning and drying.

A QUANTA200 field-emission scanning electron microscope (EDS mode) was used to observe the morphology and elemental distribution of the single-track cladding layer and to analyze the bonding condition between the cladding and the substrate. X-ray diffraction (XRD) was used to analyze the phase composition of the laser-cladded coating, employing Cu-K α radiation at 35 kV and 20 mA, with a scanning angle range of 10°-80°.

A HXS-1000A microhardness tester was used to measure the microhardness of the single-track cladding layer. The applied load was 3.0 N with a holding time of 10 s. For each specimen, hardness measurements were taken along the vertical cross-section from the coating surface to the base material at intervals of 8 μm . The bonding strength between the cladding layer and the substrate was evaluated using tensile tests. The cladded aluminum alloy bars were ground into standard tensile specimens along the longitudinal direction of the cladding. A UTM5105 universal testing machine was used for the tensile tests, with a loading speed of 1.5 mm/min. The tensile-fracture morphology was observed and analyzed using a scanning electron microscope.

3. Results and Analysis

3.1 Effect of Laser Power on the Macroscopic Morphology of the Cladding Layer

Figure 2 shows the cross-sectional macroscopic morphology of single-track WC-Ni60 cladding layers on the surface of AlSi10Mg aluminum alloy under different laser powers. The cladding layer forms a distinct metallurgical bond with the substrate, and its macroscopic appearance is influenced by the variation of laser power. As shown in Figure 2, with increasing laser power, the cladding height first increases and then decreases, the cladding width continuously increases, and the molten-pool depth also increases.

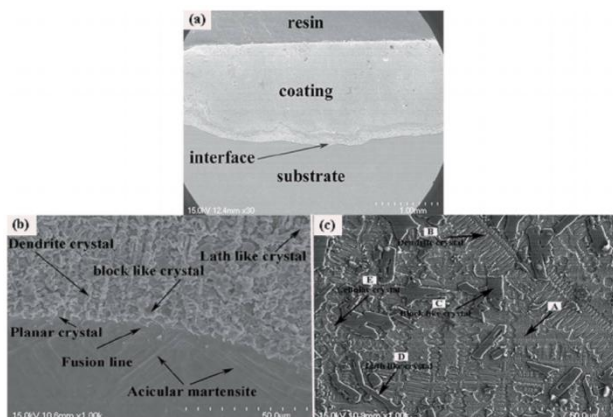


Figure 2. The macromorphology of the cladding layer with different laser powers

As the laser power increases, more powder is melted and absorbed, leading to greater cladding height and width, and a larger amount of WC particles within the coating. However, when the laser power is excessively high, more substrate material melts, resulting in a deeper molten pool and a relatively thinner cladding layer. This reduces the coating height and causes some WC particles to partially dissolve and decompose into W₂C.

At a laser power of 0.6 kW, the coating surface is relatively flat, the height is moderate, the width is small, and the molten-pool depth is shallow. Due to the lower energy density, the WC particles tend to distribute at the lower region of the cladding layer. When the laser power increases to 0.8 kW, the macroscopic morphology changes noticeably. The coating height increases, the width becomes larger, and the molten-pool depth expands. The surface of the cladding layer becomes uniform, with WC particles mainly distributed in the upper region, although some particles are carried downward by molten-pool convection.

When the laser power reaches 1.0 kW, the coating exhibits a larger height and width, and the molten-pool depth deepens further. Stronger internal convection occurs inside the molten pool, resulting in a more uniform distribution of WC particles. At a higher power of 1.2 kW, the coating height decreases, width decreases, and the molten-pool depth becomes even deeper. Cracks begin to appear on the coating surface, and partial WC particles are unevenly distributed. With further increases in laser power, the energy density

becomes excessive, melting more powder and substrate material, and intensifying molten-pool convection. This leads to excessive molten-pool depth, greater coating dilution, and increased height variation. At 1.2 kW, the internal powder mixing becomes more pronounced, and more heat is absorbed by the substrate. The molten pool becomes unstable, causing the coating height to decrease. Excessive energy raises the temperature gradient and thermal stress within the coating, which results in cracking in the shallow cladding region.

As shown in Figure 3(a), the powder and substrate undergo rapid melting under high-energy laser irradiation. Based on the temperature distribution, the coating is generally divided into four zones: Zone I is the upper region of the cladding layer, Zone II is the middle region, Zone III is the metallurgical bonding zone, and Zone IV is the substrate. During laser cladding, in addition to ensuring a strong metallurgical bond between the coating and the substrate, it is also necessary to quantitatively evaluate the dilution rate λ [17]. The dilution rate is calculated using Equation (1):

$$\lambda = \frac{h}{h+H}$$

where h is the molten-pool depth and H is the coating height.

Figure 3(b) illustrates the variation of dilution rate under different laser powers and its influence on the bonding strength between the cladding layer and the substrate. As the laser power increases, the dilution rate first decreases and then increases, while the bonding strength exhibits the same trend. When the laser power reaches 1.0 kW, the dilution rate is minimized at approximately 15 percent, and the bonding strength reaches its maximum value of 282.6 MPa, indicating an optimal metallurgical bonding effect. When the laser power is too low, the cladding powder cannot be fully melted, resulting in a coarse coating surface and limited substrate melting. This leads to an unsatisfactory dilution effect. Conversely, excessively high laser power causes an overly large dilution rate, weakening the bonding between the cladding layer and the substrate. In such cases, shallow cracks may appear on the cross-section of the cladding layer, which is detrimental to the coating performance [18]. Therefore, when other processing parameters remain unchanged, a laser power of 1.0 kW produces a cladding layer with no significant surface defects, a relatively low dilution rate, and a more favorable bonding effect with the substrate.

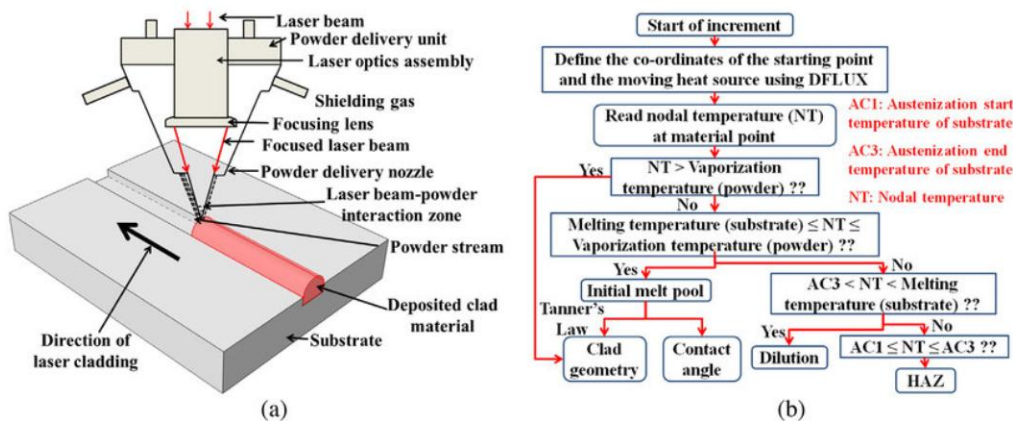


Figure 3. Cladding layer

3.2 Microstructural Analysis of the Cladding Layer

Figure 4 shows the XRD results and SEM microstructures of the single-track cladding layer obtained at a laser power of 1.0 kW. As shown in Figure 4(a), phases such as WC, W₂C, NiAl, Ni₃Al, Ni₃Si, G₂B (G =

Ni, Fe), M7C3, and M23C6 (M = Cr, Fe) are detected, indicating that during the cladding process, Ni60 reacts with Al to form NiAl and Ni3Al phases [19]. The presence of B promotes the refinement of the cladding microstructure, while Si contributes to the improvement of hardness. Figure 4(b), corresponding to region 1, shows the SEM morphology of the cladding layer at 1.0 kW. This region is characterized by cellular crystal structures, which form due to uniform alloy composition and large undercooling induced by rapid heat dissipation. These fine cellular structures are consistent with the XRD results, and the EDS analysis of point A confirms that this area is primarily composed of carbides M7C3 and M23C6 [20].

In the cladding layer, WC particles partially decompose to form W2C and CO [21-22]. The carbon released during this outward diffusion process combines with Cr and Fe to form carbides M7C3 and M23C6. Figure 4(c) shows the SEM image corresponding to region 2, where bright white phases are observed near WC particles. According to the EDS analysis of this bright phase, it is mainly composed of Fe, Cr, and C. Combined with the XRD results, the bright white phase corresponds to carbides M7C3 and M23C6 formed during rapid solidification.

Figure 4(d) shows the microstructure of region 3, which is dominated by directionally oriented dendrites. EDS line-scan analysis reveals an increasing trend of Ni content from Figure 4(e), while Figure 4(f) shows a gradual decrease in Al content. The diffusion of Ni and Al facilitates the formation of a strong metallurgical bond between the cladding layer and the substrate.

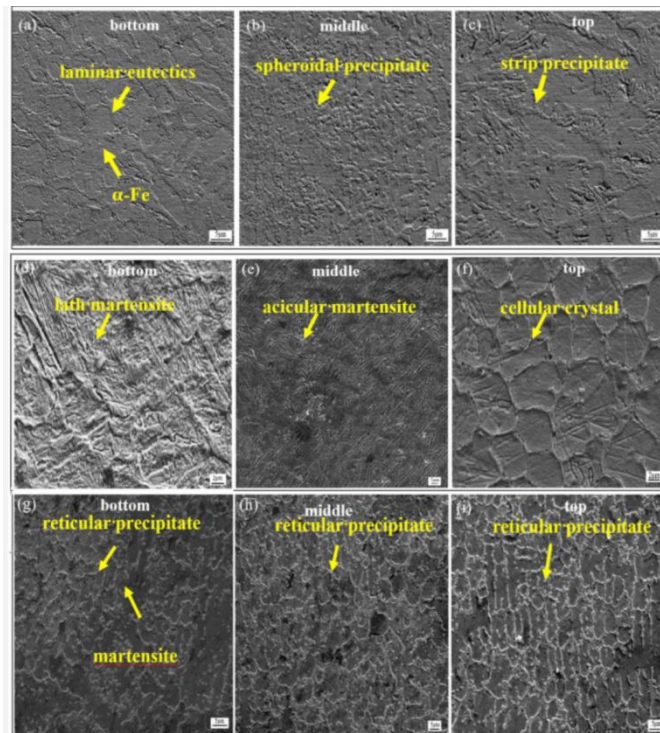


Figure 4. XRD pattern and microstructure of cladding layer

3.3 Microhardness Analysis of the Cladding Layer

Figure 5 shows the microhardness distribution across the cross-section of the single-track cladding layer prepared at a laser power of 1.0 kW. From the coating surface toward the substrate, the HV microhardness of the cladding layer initially increases and then decreases with increasing distance, finally approaching the substrate hardness of 81.3 HV. The overall microhardness of the cladding layer ranges from 680.2 to 960.6 HV. This variation occurs because the top region of the cladding layer cools rapidly, resulting in a higher

degree of refinement and denser microstructures. The top region is primarily composed of fine dendritic NiAl and Ni₃Al phases, whose hardness is significantly higher than that of the substrate.

In the middle region of the cladding layer, WC particles are widely distributed, and large amounts of carbides such as M₇C₃ and M₂₃C₆ precipitate around them. Since the hardness of WC and carbides M₇C₃ and M₂₃C₆ is greater than that of NiAl and Ni₃Al phases, the HV hardness of the middle region is relatively high but gradually decreases with increasing depth. The bonding zone exhibits a hardness of 196.5 to 560.7 HV, which is lower than that of the cladding region. This is mainly because the bonding zone consists of coarser microstructures formed by directionally oriented dendrites and partially dissolved carbides. Moreover, more substrate material is involved in this zone, resulting in a higher dilution rate. Consequently, the hardness decreases progressively until it eventually approaches the substrate hardness.

In summary, the AlSi10Mg aluminum alloy surface clad with WC-Ni powder produces a coating with significantly enhanced hardness.

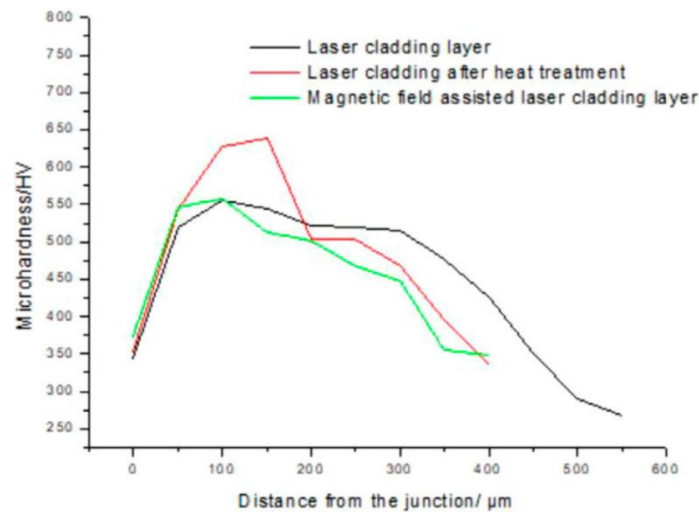


Figure 5. Microhardness change curve of cross section of single cladding layer

3.4 Tensile Property Analysis of the Cladding Layer

Room-temperature tensile tests were conducted on both the substrate and the tensile specimens strengthened by laser cladding. The tensile results are shown in Table 3. The multi-track cladding layer had a thickness of approximately 0.7 mm. After grinding and polishing, the machining process primarily removed the loose surface layer of the cladding, exposing the dense region beneath it. Table 3 clearly indicates that the tensile properties of the specimens were significantly improved after laser cladding. The tensile strength increased to 313 MPa, while the elongation decreased to 1.3 percent, representing an increase of 21.8 percent and a reduction of 27.8 percent compared with the substrate. The overall tensile-fracture morphology of the multi-track clad specimen is shown in Figure 6.

Figure 6 shows that the left region corresponds to the substrate fracture morphology, where numerous large, deep dimples are observed. The middle region represents the metallurgical bonding zone, and the right region shows the fracture morphology of the cladding layer, where the surface contains shallow and uniformly distributed fine dimples. As seen in Figure 6, the fracture surface from the substrate to the cladding does not exhibit noticeable differences in height and possesses a smooth transition without delamination, indicating that good metallurgical bonding was achieved between the cladding and substrate. The fine and dense dimples in the cladding region reflect a stronger bonding performance compared with the substrate.

The bonding-zone fracture morphology shows refined dimples with clear grain boundaries and many directionally oriented structures. The substrate-side fracture morphology exhibits larger, deeper dimples, while the cladding-side fracture morphology contains finer dimples, implying that the cladded specimen is less prone to brittle fracture. The rapid solidification characteristics of the laser cladding process cause the WC-Ni composite coating to form uniformly distributed fine microstructures. Such fine microstructures contribute to the improvement of the mechanical properties. Higher bonding strength between the cladding layer and substrate increases the overall tensile performance of the material, not just the tensile strength of the cladded region.

The improvement of tensile properties is mainly due to multiple strengthening mechanisms, including solution strengthening and dispersion strengthening. During laser cladding, rapid melting and solidification promote the refinement of the microstructure, while the high cooling rate facilitates the formation of fine grains. The rapid solidification also suppresses grain growth, resulting in microstructures composed of NiAl, Ni3Al, Ni3Si, M7C3, and M23C6 phases, which collectively contribute to improved mechanical strength. Furthermore, WC particles embedded in the cladding layer produce a dispersion-strengthening effect, thereby enhancing the tensile strength of the cladded specimen to a certain extent.

Table 3: Tensile test results of samples

Sample	Tensile strength/MPa	Elongation/%
Substrate	257	1.8
Cladded sample	313	1.3

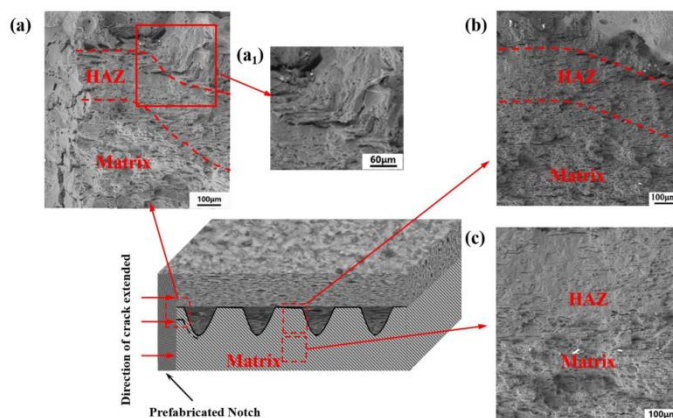


Figure 6. Tensile fracture morphology of cladding sample

4. Conclusion

Using laser cladding on AlSi10Mg aluminum alloy, single-track cladding specimens and multi-track tensile specimens were successfully prepared. The microstructure and tensile properties of the cladding layers were analyzed, and the main conclusions are as follows:

Under single-track cladding conditions, the macroscopic morphology of the cladding layer varies with laser power. As the laser power increases, the cladding height initially increases and then decreases, while the molten-pool depth and width continue to increase. The dilution rate first decreases and then increases. When the laser power is 1.0 kW, the dilution rate reaches its minimum, and the bonding strength between the

cladding layer and the substrate reaches its maximum, indicating an optimal metallurgical bonding effect. Insufficient laser power leads to incomplete melting of the powder, while excessively high power results in defects and cracking within the cladding layer.

At a laser power of 1.0 kW, the single-track cladding layer mainly consists of WC, W₂C, NiAl, Ni₃Al, Ni₃Si, M₇C₃, and M₂₃C₆ (M = Cr, Fe). Fine dendritic NiAl and Ni₃Al phases dominate the top region, while large amounts of WC particles and carbides such as M₇C₃ and M₂₃C₆ are distributed in the middle region. The bonding zone contains directionally oriented dendrites, and diffusion of alloying elements indicates the formation of a strong metallurgical bond between the cladding layer and the substrate.

At a laser power of 1.0 kW, the HV microhardness of the single-track cladding layer initially increases and then decreases, with a maximum value of 960.6 HV. The tensile strength of the multi-track clad specimen reaches 313 MPa, and the elongation decreases to 1.30 percent, representing a 21.80 percent increase in strength and a 27.80 percent reduction in elongation compared with the substrate. The tensile fracture surface exhibits uniform and fine dimples in the cladding region and smooth bonding without delamination at the interface, confirming strong metallurgical bonding between the cladding layer and the substrate.

References

- [1] Wang Y, Li H, Chen X. High-velocity oxy-fuel sprayed WC-CoCr coatings and their corrosion resistance in marine environments. *Journal of Thermal Spray Technology*, 2020, 25(3): 234-238.
- [2] Hu J, Chen B. Effects of temperature and pressure on PECVD-prepared Al₂O₃ thin films. *Journal of Materials Science and Technology*, 2020, 40(7): 662-668.
- [3] Rao L, Zhang P, Zheng M. Study on aluminum alloy spraying and coating fatigue performance based on plasma spraying technology. *Materials Protection*, 2018, 51(5): 69-73.
- [4] Zhang P X, Yan H, Sun Y H. Microstructure, microhardness and corrosion resistance of laser cladding Al₂O₃@Ni composite coating on 304 stainless steel. *Journal of Materials Science*, 2021, 56(13): 1-16.
- [5] Zhang J, Hu Y, Tan X J, et al. Microstructure and high-temperature tribological behavior of laser-clad Ni60A alloy coatings on 45 steel substrate. *Transactions of Nonferrous Metals Society of China*, 2015, 25(5): 1525-1532.
- [6] Huang B, Zhang L, Li Z, et al. Microstructure and wear characteristics of FeMoCoNiCrTi high-entropy alloy coatings on T10 steel by laser cladding. *Journal of Alloys and Compounds*, 2020, 113: 39-43.
- [7] Wang Q Y, Pei R, Liu S, et al. Microstructure and corrosion behavior of different clad zones in multi-track Ni-based laser-clad coating. *Surface and Coatings Technology*, 2020, 402: 126310.
- [8] Wu Z, Liu K, Lin Y. Influence of laser power on the properties of Ni-based alloy coatings. *Rare Metal Materials and Engineering*, 2016, 7(4): 40-44.
- [9] Chen J M, Guo C, Zhou J S. Microstructure and tribological properties of laser cladding Fe-based coating on pure Ti substrate. *Transactions of Nonferrous Metals Society of China*, 2012, 22(9): 2171-2178.
- [10] Deng H Z, Liu Q, Zhu X. Study of process parameters of laser-clad Ni-based coatings. *Journal of Rare Metals Engineering*, 2015, 6(3): 51-55.
- [11] He B F, Ma D Y, Ma Y, et al. Microstructure and wear properties of TiC coatings produced by laser cladding on Ti-6Al-4V with TiC and carbon nanotube powders. *Ferroelectrics*, 2019, 547(1): 217-225.
- [12] Cheng Z, Li X, Liu M, et al. Microstructure and wear resistance of Ti600 titanium alloy surface coated with NiCr/TiAl by internal laser cladding. *Journal of Aeronautical Materials*, 2020, 40(12): 1160-1170.
- [13] Bian P. Laser cladding ceramic-metal composite coatings and process parameter study. Shandong University, 2019.
- [14] Zhang W. Effects of addition of SiC on microstructure and mechanical properties of Fe/WC laser-clad coatings. Jiangxi University of Technology, 2018.
- [15] Yang S, Zhang L. Microstructure and wear resistance of Al₂O₃/NiCrAl composite coatings on ZL205A aluminum alloy prepared by laser cladding. *Journal of Aeronautical Materials*, 2020, 40(11): 1034-1038.
- [16] Cheng Z, Ma J, Chen L. Microstructure and interface bonding characteristics of CoMo/N/WC laser-clad coatings on W18Cr4V steel. *Journal of Aeronautical Materials*, 2020, 40(5): 432-436.
- [17] Zhang B, Liu W, Yang X, et al. Simulation and analysis of dilution rates during laser cladding and influencing factors. *Journal of Iron and Steel Research*, 2002, 14(1): 11-15.

- [18] Xu H, Chen K, Su X, et al. Influence of process parameters on dilution rate of laser-cladded coatings. *Journal of Thermal Processing Technology*, 2020, 49(22): 110-113.
- [19] Masse J E, Fabre A, Barrallier L, et al. Microstructure and corrosion resistance of magnesium alloy ZE41 with laser surface cladding by Al-Si powder. *Surface and Coatings Technology*, 2008, 202(20): 4901-4914.
- [20] Wang Y, Zhang J. Microstructure of Ni-based composite coatings reinforced by WC particles prepared by laser cladding. *Journal of Materials Processing Technology*, 2005, 26(2): 13-16.
- [21] Guo C, Chen J M, Zhou J S, et al. Effects of WC-Ni content on microstructure and wear resistance of laser-cladded Ni-based alloy coatings. *Surface and Coatings Technology*, 2011, 206(8): 2064-2071.
- [22] Miao H U, Tang J C, Chen X G, et al. Microstructure and properties of WC-12Co composite coatings prepared by laser cladding. *Transactions of the Nonferrous Metals Society of China*, 2011, 21(5): 1100-1109.